RSC Advances

ROYAL SOCIETY OF CHEMISTRY

PAPER

View Article Online
View Journal | View Issue

Check for updates

Cite this: *RSC Adv.*, 2024, **14**, 39759

Insights into ESIPT-induced multicolor fluorescence emission in 2-(2′-hydroxy-5′-bromo)phenylbenzimidazole: a spectroscopic and TDDFT study†

Yumeng Wang,‡[a] Mingxia Hu,‡[a] Qianqian Yue,[a] Feng Xiaoqing[b] and Yanying Zhao *[a]

Received 25th August 2024
Accepted 28th November 2024

DOI: 10.1039/d4ra06147k

rsc.li/rsc-advances

Although multicolor luminescent materials are widely used in information encryption and decryption based on the excited-state intramolecular proton transfer (ESIPT) reaction, there remains a significant gap in the mechanistic understanding of how solvent and pH conditions influence the ESIPT process. Owing to their ability to avoid self-absorption as well as provide large Stokes' shift and strong emission properties, ESIPT-generated molecules (ESIPT gens) have recently emerged as highly potential fluorophores. Herein, the ESIPT mechanism of bromine-based (2′-hydroxy-5′-bromo)phenylbenzimidazole (**HBI-pBr**) was investigated in solvents using spectroscopic measurements and time-dependent density functional theory (TD-DFT) calculations. The results indicated that multi-color fluorescence emissions were observed at 470, 458 and 416 nm in CH_3OH doped with a base and acid. The potential energy profile rationalized the fluorescence mechanistic insights into the ESIPT reaction and pH-dependent dual response. Notably, nucleus-independent chemical shift (NICS_ZZ) values were applied to reveal the ESIPT process. We leveraged the bromine atom as an electron withdrawing group to manipulate ground and excited-state proton transfer, thereby offering a strategic approach for designing and developing an ESIPT fluorescence sensor for the detection of H^+ and OH^-. By studying the effect of solvent and pH conditions on **HBI-pBr**, the multicolor fluorescence mechanism of ESIPT was elucidated, thus laying a solid foundation for the design and synthesis of luminescent materials based on the ESIPT reaction.

Introduction

Excited-state intramolecular proton transfer (ESIPT) routinely results in a large Stokes' shift and even strong fluorescence emission, effectively avoiding interference from self-absorption and inner-filter effects.[1–3] Intramolecular hydrogen bonds play a crucial role in ESIPT reactions and contribute to enhancing photostability as the typical photoacid.[4–6] Based on the characteristic four-level-energy photochemical cycle (enol → enol* → keto* → keto), the ESIPT molecules are utilized as fluorescent probes for biomarker detection,[7–9] optoelectronics for lasers,[10] OLEDs[11,12] and anticounterfeiting encryption materials,[13,14] including Förster resonance energy transfer (FRET),[15] intramolecular charge transfer (ICT),[16,17] multi-proton transfer,[18–20] and aggregated-induced emission (AIE)[21] coupled with ESIPT. More interestingly, ESIPT probes exhibit high sensitivity for detecting and visualizing metal ions, SO_2, H_2O_2 and other molecules.[22–26] Furthermore, sensitivity to the environment, such as solvent and pH, can promote multicolor fluorescence emission.[27–30]

Excited-state proton transfer in 2-(2′-hydroxy)phenylbenzimidazoles (HBIs), a fascinating and typical ESIPT-generated molecule (ESIPT gen), is of utmost importance in chemistry and materials. The intricate process is understood through a combination of spectroscopic methods and time-dependent density functional theory (TDDFT).[31–34] The proton transfer (PT) requires a proton-donating entity (–OH, >NH and –NH_2) and a proton-accepting entity (=N– and –C=O), which effectively enhance the fluorescence quantum yield.[35,36] Furthermore, HBI derivatives display the nature of fluorescent probes owing to the smart sensing of Zn^{2+} and Al^{3+} based on the ESIPT reaction mechanism.[37,38] Additionally, HBI derivatives demonstrate multi-color fluorescent and pH-dependent fluorescence properties due to special substituents.[39] Thus, substituted functional groups in HBIs enable the fine-tuning of

---

[a] School of Chemistry and Chemical Engineering, School of Materials Science and Engineering, Zhejiang Sci-Tech University, Hangzhou 310018, China. E-mail: dameng0902@163.com; H_mx469@outlook.com; 1326443499@qq.com; yyzhao@zstu.edu.cn

[b] School of Pharmacy, School of Medicine, Changzhou University, Changzhou 213164, China. E-mail: fxq@163.com

† Electronic supplementary information (ESI) available. See DOI: https://doi.org/10.1039/d4ra06147k

‡ Contributed equally by Mingxia Hu and Yumeng Wang.

their photophysical and photochemical properties, providing a strategy for designing and developing luminescent materials while improving and even mediating efficient fluorescent quantum yields.[40] In particular, heavy atoms in HBIs, such as Br and S, can shift emission pathways from fluorescence emission to intersystem crossing (ISC).[41,42]

Herein, an ESIPT-based multicolor fluorescence molecule was initially synthesized *via* the introduction of a bromine atom on the *p*-substituted position of hydroxyl group 2-(2′-hydroxy)phenylbenzimidazole (HBI), as shown in Scheme 1(a). Combined with density functional theory (DFT) and time-dependent density functional theory (TDDFT) calculations, we revealed the multicolor fluorescence mechanism through the spectroscopic experiments, potential energy profiles and nucleus-independent chemical shift (NICS(1)_ZZ) values, which are key indicators of aromaticity (negative values) and anti-aromaticity (positive values).

Experimental and computational methods

The synthesis route of 2-(2′-hydroxy-5′-bromo)phenylbenzimidazole (**HBI-pBr**) is shown in Scheme 1(a) and detailed in the ESI.†[43] Fig. S1† shows the ^{1}H NMR spectrum (400 MHz, DMSO-d_6) δ 13.32 (s, 2H), 8.32 (d, $J = 2.5$ Hz, 1H), 7.71 (s, 2H), 7.55 (dd, $J = 8.8$, 2.5 Hz, 1H), 7.37–7.30 (m, 2H), and 7.05 (d, $J = 8.8$ Hz, 1H). Various concentrations of **HBI-pBr** were prepared using high-performance liquid chromatography grade acetonitrile (99.9%, Tedium Company, Inc., USA), methanol, cyclohexane, dichloromethane, tetrahydrofuran, and dimethyl sulfoxide (both 99.9%, Spectrum Chemical Mfg. Corp., USA). UV absorption spectra were measured in cyclohexane, dichloromethane, tetrahydrofuran, methanol, acetonitrile and dimethyl sulfoxide at concentrations of $\sim 10^{-5}$ mol L^{-1} using a UV-visible spectrometer (UV-2501PC, Shimadzu Corp., Japan). Fluorescence emission spectra were recorded using an F-4600 FL spectrophotometer at the same concentration.

Density functional theory (DFT) calculations were performed to acquire the ground geometries.[44–46] The vibrational analysis was carried out at the same level of theory as geometry optimization to identify the characteristics of all the obtained stationary points (minima and transition states). To obtain the minima of the excited state, a time-dependent DFT (TD-DFT) calculation was performed at the B3LYP functional.[47–55] The 6-311+G(d, p) basis was applied for all elements for both the DFT and TD-DFT calculations.[56] The solvation energies were evaluated using the polarized continuum model (PCM).[57] The intrinsic reaction coordinate (IRC)[58] calculations were analyzed to confirm the transition states connecting the corresponding reactant and product in Scheme 1(b). The NICS values were computed as 1 Å above the ring center along the ZZ axis based on the ZZ component of the nuclear shielding tensor at that point.[59,60] Notably, Baird's rule[61] elucidates the molecular behavior in the triplet excited state (T$_1$), where molecules that are aromatic in the ground state (S$_0$) become antiaromatic in T$_1$, and *vice versa*. This principle has been extended to encompass the singlet excited state (S$_1$). Schleyer *et al.*[62] proposed that negative NICS(1)_ZZ values indicate S$_0$ aromaticity, with more negative values correlating to stronger aromaticity, while positive values suggest *anti* aromaticity. Recent studies have shown

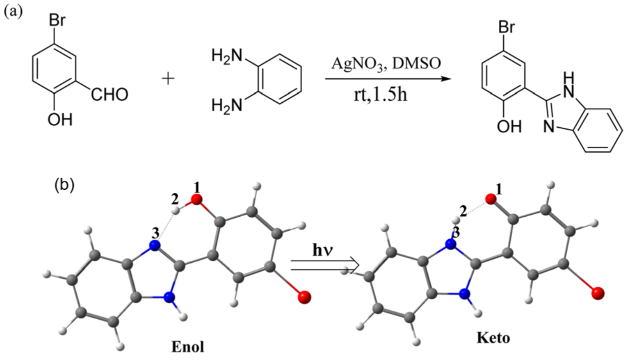

Scheme 1 Synthesis route (a) and structural tautomers (b) of **HBI-pBr**.

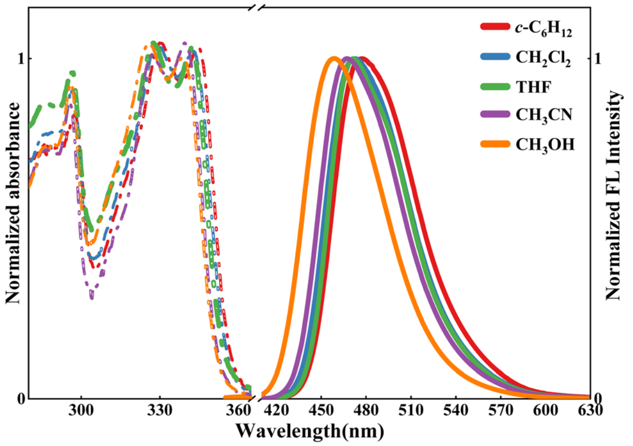

Fig. 1 Normalized absorption (dotted) and fluorescence spectra (solid, $\lambda_{ex} = 340.0$ nm) in cyclohexane (c-C_6H_{12}), dichloromethane (CH_2Cl_2), tetrahydrofuran (THF), acetonitrile (CH_3CN) and methanol (CH_3OH).

Table 1 Experiments in different solvents and calculated λ_{abs}^{max}/nm, λ_{em}^{max}/nm and Stokes' shift ($\Delta\nu$)/cm^{-1} of *cis*-phenol and keto **HBI-pBr** in different solvents

	λ_{abs}^{max}/nm [a]		λ_{em}^{max}/nm [b]		
Solvent	Exp	Cal	Exp	Cal	$\Delta\nu$ (cm^{-1}) [c]
Cyclohexane	344	333	477	454	8105(8004)
Dichloromethane	342	329	473	432	8098(7247)
Tetrahydrofuran	342	329	472	433	8053 (7300)
Acetonitrile	340	327	468	428	8044 (7217)
Methanol	338	327	458	428	7752(7217)

[a] Calculated at TD-B3LYP/6-311+G(d, p) on optimized S$_0$ at the B3LYP/6-311+G(d, p) level using the corresponding PCM solvent model. [b] Calculated at TD-B3LYP/6-311+G(d, p) on optimized S$_1$ at the TD-B3LYP/6-311+G(d, p) level using the corresponding PCM solvent model. [c] Data in parentheses calculated Stokes shift.

Table 2 Bond distance (Å) and bond angle (°) of ground and excited phenol and keto isomers optimized at the B3LYP-TD/6-311+G(d, p) level using the PCM (solvent = methanol) model

	Species			
	Phenol		Keto	
Distance	$S_{0,min}$	$S_{1,min}$	$S_{0,min}$	$S_{1,min}$
O1–H2	0.998	1.015	1.742	1.974
H2–N3	1.690	1.639	1.036	1.016
δ(O1–H2–N3)	148.3	150.2	133.4	124.0

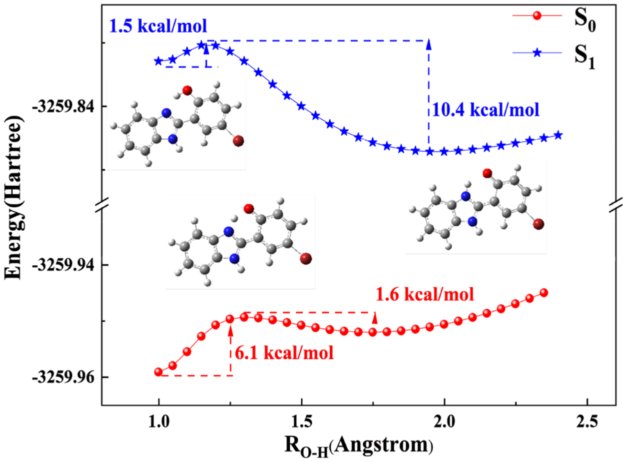

Fig. 2 Potential energy curves for the S_0 and S_1 states of **HBI-pBr** calculated at the TD-B3LYP/6-311+G(d, p) level (step size 0.05 Å) using PCM (solvent = methanol) model.

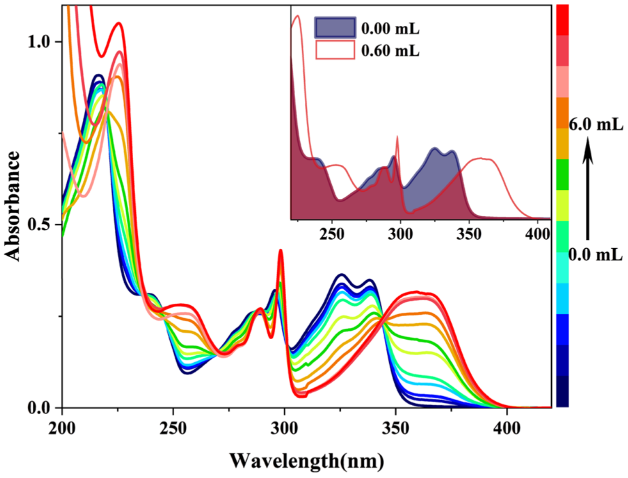

Fig. 3 UV spectra of a 2.5 × 10^{-5} M **HBI-pBr** solution in CH_3OH as a function of 2.0 × 10^{-4} M [(Bu)4N]OH solution in CH_3OH. The absorbance evolution of **HBI-pBr** upon increasing concentration $[(Bu)_4N]OH$ from 0 to 6.00 mL.

that changes in NICS(1)_ZZ during the ESIPT signal reduce aromaticity, driving the ESIPT process.[63,64]

All DFT and TD-DFT calculations were carried out using the Gaussian 09 program package.[65]

Results and discussion

Fig. 1 shows the UV-Vis absorption and fluorescence emission spectra in five solvents. In the 300–360 nm region, two shoulder absorption peaks were observed at ~340 and 330 nm, displaying the solvent-dependent shift. As shown in Table 1, the absorption band was observed at 344 nm in c-C_6H_{12}, while in CH_3CN and CH_3OH, it shifted to 339.6 and 338 nm, respectively. Simultaneously, similar absorptions were observed at 342.4 and 342 nm in CH_2Cl_2 and THF, respectively. The above-mentioned results indicated that the maximum absorption peaks are blue-shifted with increasing solvent polarity.[66,67]

To further interpret the experimental results, four ground configurations, *cis*-phenol, *trans*-phenol, *cis*-phenol-1, and keto in CH_3OH were optimized at B3LYP-TD/6-311+G(d, p) level. As shown in Fig. S2,† the *cis*-phenol isomer is the most stable, while both keto and *trans*-phenol are about 6.5 kcal mol^{-1} higher energy. Table S2† indicates the vertical transition energies calculated using the corresponding solvent model. The transition energy at 332 nm for the *cis*-phenol aligns well with the experimentally observed shoulder absorptions at 344 and 330 nm, which mainly corresponds to the π → π* transition. The additional maximum absorption bands observed at 298 and 288 nm also matched the calculated values at 287 and 283 nm. As shown in Table S2,† the absorption band at 330 nm seems close to the calculated electronic transition of the *trans*-phenol at 323 nm. However, the potential energy profile scan indicates that the torsional process from *cis*-phenol to *trans*-phenol requires a barrier of 10.4 kcal mol^{-1}, while the reverse barrier is only 5.4 kcal mol^{-1} along the dihedral angle of $D_{15\text{-}13\text{-}7\text{-}21}$, as shown in Fig. S3.† Thus, *cis*-phenol is the dominant isomer, both thermodynamically and kinetically.[68,69]

From Fig. 1, when excited at 340 nm, **HBI-pBr** exhibits the solvent-dependent emission observed at 477 nm in c-C_6H_{12}, 473 nm in CH_2Cl_2, 472 nm in THF, 468 nm in CH_3CN and 458 nm in CH_3OH. As illustrated in Tables 1 and S1,† the Stokes' shift exhibits a negative correlation with the solvent polarity.[70] Table S1† indicates that *para*-bromine substitution modulates the proton transfer dynamics and charge transfer efficiency likely through its influence on electronic distribution and steric factors. The lowest unoccupied molecular orbital (LUMO) is more localized than the highest unoccupied molecular orbital (HOMO). With a bromine (Br) atom at the tip apex, there is a pronounced localization of electron density within the phenol group (fragment 2), particularly evident in the LUMO. As an electron-attracting group, the bromine atom causes the electron density to concentrate more within the phenol group, as opposed to the more balanced charge transfer in HBI. The reduction in the HOMO–LUMO charge distribution gap from 6.0% in HBI to 1.5% in **HBI-pBr** further validates that bromine substitution enhances electron localization and diminishes intramolecular charge transfer (ICT), inhibiting charge transfer with minimal impact on the emission spectrum.[71,72]

Subsequently, TD-DFT calculations were applied to identify the electronic spectrum. The calculated emission band at 454 nm for keto **HBI-pBr** corresponds well with the

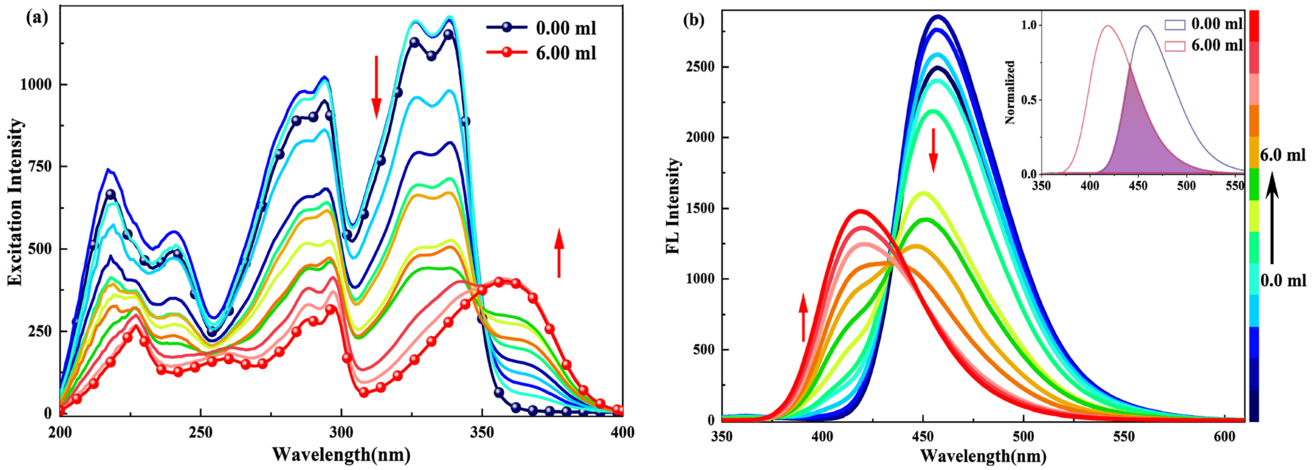

Fig. 4 (a) Excitation ($\lambda_{em} = 419.0$ nm) and (b) emission spectra ($\lambda_{ex} = 340.0$ nm) of 2.5×10^{-5} M **HBI-pBr** in CH_3OH as a function of 2.0×10^{-4} M $[(Bu)_4N]OH$ solution in CH_3OH from 0 to 6.00 mL.

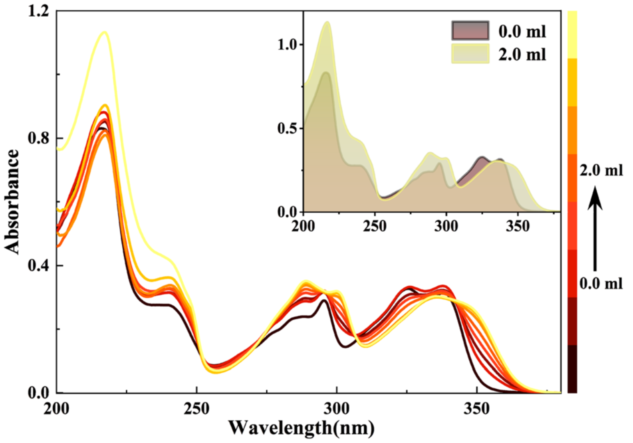

Fig. 5 UV-Vis spectra of a 2.5×10^{-5} M **HBI-pBr** solution in CH_3OH as a function of CF_3COOH (TFA, 2.0×10^{-4} M) in CH_3OH from 0 to 2.00 mL.

experimental emission band at 477 nm in c-C_6H_{12}, as shown in Table 1. Similarly, the calculated emission bands in the other four solvents also align well with the experimental data illustrated in Table 1. Relatively large Stokes' shifts were observed in c-C_6H_{12} compared to the other solvents. Table 2 compares the bond distances of O1–H2 and H2–N3, and the bond angles of O1–H2–N3 in both the ground and first singlet excited states. For phenol, the O1–H2 bond length was elongated from 0.998 Å in S_0 to 1.015 Å in S_1, while the distance of H2–N3 was shortened from 1.690 Å in S_0 to 1.639 Å in S_1. The above-mentioned results indicate that **HBI-pBr** is a characteristic of photoacid, similar to HBO.[73] For keto, the H2–N3 bond length further decreased from 1.036 Å in S_0 to 1.016 Å in S_1, while the O1–H2 bond increased by 0.232 Å in S_1. δ(O1–H2–N3) angle was largest in S_1 for phenol, while a compact S_1 of keto structure perhaps is attributed to the smallest δ(O1–H2–N3). Photoisomerization between *cis*-phenol and keto is calculated along the O1–H2 bond distances, and the potential energy curves of the ground and first singlet excited states are also shown in Fig. 2. The energy barrier of PT is 6.1 kcal mol^{-1} in S_0 along the O1–H2 bond, which, however, reduces to only 1.5 kcal mol^{-1} in S_1. More importantly, the energy barrier on S_1 reaches 10.4 kcal mol^{-1} from keto to *cis*-phenol, contrary to S_0.[74–76] Thus, the ESIPT reaction is validated both thermodynamically and kinetically. Fig. S4† shows the natural atom charge on S_1 and S_0 of the phenol and keto forms. For phenol, the charges on O1 and N4 are −0.710 and −0.531 in S_0 and -0.707 and −0.524 in S_1, respectively, indicating a slight decrease in the negative charge excited state. Meanwhile, the positive charges on H2 and H5 increase by 0.001 and 0.022, respectively, from S_0 to S_1 states, with the H2 proton showing greater photoacidity than the H5 proton. Thus, H2 has perhaps stronger photoacidity than H5. However, for keto, the positive charges on H5 are consistently 0.433 larger than those in the phenolic structure, making H5 protons more likely to be deprotonated by OH$^-$, which facilitates the formation of an anion. These findings are in accordance with the significant charge redistribution upon excitation, enhancing the molecule's polarity. Consequently, we can comprehensively investigate the photophysical process of **HBI-pBr** in relation to base concentration, enabling us to conduct analogous spectral measurements with enhanced precision.

When doped with $[(Bu)_4N]OH$ in **HBI-pBr**/CH_3OH, as shown in Fig. 3, a series of new absorption bands were generated at 363/360, 298, 289, 253 and 225 nm, displaying significant blue shifts compared to the absorption bands at 338/326, 296, 286, 236 and 217 nm observed in pure CH_3OH, respectively. Fig. 4(a) further highlights new bands observed around 360, 300, 260, and 220 nm, close to the absorption bands mentioned. A new fluorescence emission band is observed at 416 nm excited by 340 nm for **HBI-pBr**/CH_3OH solution doped with $[(Bu)_4N]OH$, as shown in Fig. 4(b). This indicates a shift from the emission band at 458 nm observed in pure CH_3OH. These newly observed absorption and emission bands are tentatively attributed to the corresponding anions formed in the solution. Given the presence of multiple active hydrogen atoms of the –OH and –NH–

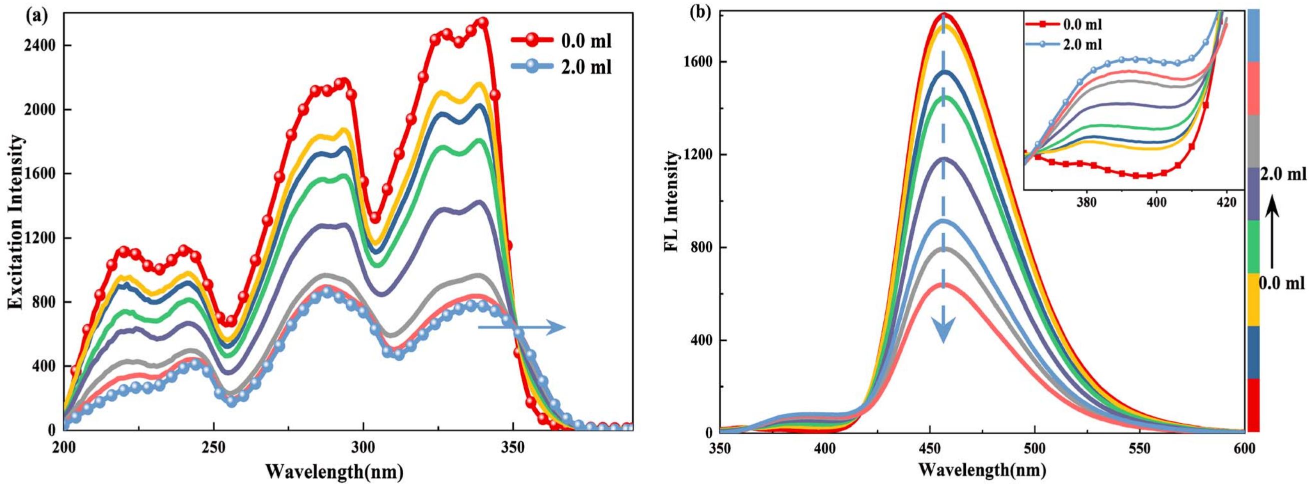

Fig. 6 (a) Excitation ($\lambda_{em} = 391.0$ nm) and (b) emission spectrum ($\lambda_{ex} = 340.0$ nm) of 2.5×10^{-5} M **HBI-pBr** in CH_3OH doped with different volumes of as a function of 2.0×10^{-4} TFA solution in CH_3OH from 0 to 2.00 mL. Note: Inset shows normalized fluorescence emission spectra from $V_{TFA} = 0$ to 2.00 mL.

Table 3 NICS(1)_ZZ values (in ppm) of possible **HBI-pBr** structures in the optimized S_0 and S_1 states calculated at the B3LYP/6-311+G(d, p) level

				Diff[b]	
System	S_0	S_1	Diff[a]	S_0	S_1
Phenol	−71.80	38.03	109.83	+10.57	−54.02
Keto	−61.23	−15.99	45.24		
Anion	−69.44	3.77	73.21	+2.36(−8.21)	−34.26(−8.21)
Cation	−69.66	10.64	80.30	+2.14(−8.43)	−27.39(+26.63)

[a] The difference of total NICS(1)_ZZ values from S_1 minus S_0 in the corresponding keto and phenol isomers. [b] The difference of total NICS(1)_ZZ values with the phenol isomer in the corresponding minima of $S_{0,min}$ and $S_{1,min}$, respectively. The values in parentheses corresponds with the keto.

groups in **HBI-pBr**, the mono- and divalent anions were optimized at the B3LYP-TD/6-311+G(d, p) level. As shown in Fig. S2,† four anionic species were identified: DA1 (proton H5 lost), DA2 (proton H2 lost), DA (divalent anion, both H2 and H5 protons lost), and DA3 (proton of H5 loss of phenolic isomer). Among these, DA1 is the most stable. Compared to DA1, a typically shorter C–O bond length of 1.268 Å exists in DA2. In contrast, DA3 has an elongated O–H bond length of 1.014 Å, together with a short N⋯H distance of 1.622 Å. The geometry of the divalent anion DA tends toward non-planarity.

As shown in Fig. S5,† the ground state DA2 can spontaneously convert to ground DA1 through a very low barrier of only 0.7 kcal mol^{-1}. Comparatively, in the first singlet excited state, the tautomeric reaction can occur from DA2 to DA1 when the barrier exceeds 8.9 kcal mol^{-1}. To sum up, it is impossible to undergo from DA1 to DA2 in either a ground or excited state. DA1 should be easily detected in the base solution.

In the excitation spectrum, as shown in Fig. 4(a), increasing $[(Bu)_4N]OH$ in CH_3OH leads to the appearance and strengthening of new bands at 358 and 343 nm, which correspond to the broad absorption band observed at ∼360/363 nm, as shown in Fig. 3. Conversely, other bands weaken and even disappear. This indicates that the structure of the excited state derived from the ground-state (DA1)[77] has changed. As depicted in Fig. 4(b), upon excitation at 340 nm, the emission peak at 458 nm gradually disappears; subsequently, a new emission peak arises at 419 nm, which originates from the absorption peak at 360 nm. Furthermore, the 419 nm emission peak aligns with the calculated emission peak at 433 nm in the S_1 state of DA1, as shown in Fig. S6(a).† Thus, *cis*-phenol **HBI-pBr** undergoes deprotonation in solution to form a monovalent anion, DA1, with maximum absorption and emission peaks at 360 and 419 nm in an alkaline environment, respectively. Perhaps, the emission spectral shift may indicate a stronger interaction between the excited **HBI-pBr** and the charged OH^- ions from $[(Bu)_4N]OH$, which we ascribe to coulomb interactions.[78]

In the excited state, the energy barriers between DA1 and DA2 are 17.0 and 8.9 kcal mol^{-1}, respectively, as shown in Fig. S5.† Compared with the ground state, both the forward and reverse barriers are enlarged in the first singlet excited state. The potential energy surface profiles indicate that large energy barriers exist for the change from DA1 to DA2 in both the ground and excited states, confirming that DA1 is the dominant species in a basic environment. To further interpret the emission, we compared the transition energy and oscillator strength (f) of DA1, DA2, DA3 and DA, as listed in Table S3.† It is found that the calculated transition energy of DA1 closely matches the experimentally observed maximum absorption. For example, the maximum absorption for DA1, calculated at 374 nm, matches well with that experimentally observed at 360 nm. Additionally, Table S4† indicates that the $S_0 \rightarrow S_1$ transition of DA1 is a typical $\pi \rightarrow \pi^*$ character with an intramolecular charge transfer (ICT) from the bromophenyl group to the benzimidazolyl unit. It is also evident that the additional

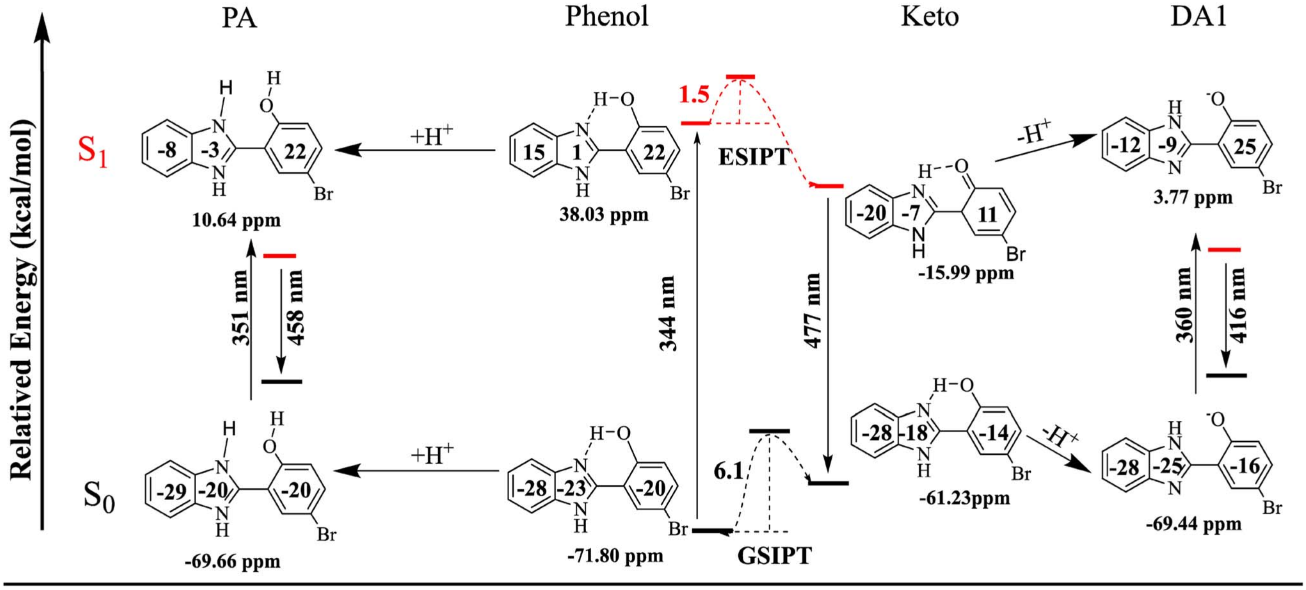

Fig. 7 Total and separately NICS(1)_ZZ values (in ppm) of **HBI-pBr** and ions in the S_0 and S_1 states and the maximal absorption and emission bands observed experimentally.

absorption peaks at 298 and 289 nm are associated with the S_4 and S_5 states, respectively.

Similarly, when doped with trifluoroacetic acid (TFA) in **HBI-pBr**/CH_3OH, a series of new absorption bands are produced at 346, 338, 300, 289, 240 and 217 nm, while the original bands at 339, 326, 296, 286, 236 and 217 nm disappear gradually, as shown in Fig. 5. Considering only one electronegative nitrogen (N3) position on the imidazole group, we tentatively identified the new species as a monovalent cation, PA. As depicted in Fig. 6(a), the excitation spectrum of **HBI-pBr** shows a broad band in the 310–370 nm region, accompanied by a pronounced tail that corresponds to the absorption band in the same region. This suggests that the excited state originates from the ground state structure, correlating with PA. As shown in Fig. 6(b), the emission peak at 458 nm gradually diminishes, while a new emission peak emerges at 391 nm in the insert of Fig. 6(b). To accurately assign the new species, DFT and TD-DFT calculations were performed to determine the stable structures and elucidate the spectral behaviour. Fig. S7† presents the optimization structures of the PA in both the ground and first excited electronic states. Table S5† lists the maximal transition energies calculated at 339, 300, 295, 236 and 218 nm, which align well with the experimentally observed peaks at 338, 300, 289, 240 and 217 nm, respectively. Table S6† demonstrates that the above-mentioned light transition is associated with the typical $\pi \rightarrow \pi^*$. As shown in Fig. S6(b),† the calculated emission peak of PA at 395 nm is consistent with that observed at 391 nm. Therefore, we can deduce that in acidic environments, **HBI-pBr** can attract one H^+ to a cationic HBO-pBr, PA.

ESIPT mechanism

To gain deeper insight into the aforementioned spectral results, NICS(1)_ZZ values are predicted, as shown in Table 3. For the ground state *cis*-phenol isomer, the value of NICS(1)_ZZ is −71.80 ppm, while the total NICS(1)_ZZ value of excited *cis*-phenol* increases to 38.03 ppm, demonstrating lower stability due to the change from aromaticity to antiaromaticity. After the ESIPT reaction, the total NICS(1)_ZZ value of the excited keto* decreases to −15.99 ppm from the *cis*-phenol*, suggesting that the ESIPT reaction in **HBI-pBr** is favorable, as it enhances stability by restoring aromaticity from antiaromaticity, consistent with Baird's rule.[61–63] This is why a large Stokes' shift is observed in **HBI-pBr**. Moreover, both the anion and cation forms of **HBI-pBr** exhibit aromaticity in the ground state, with the total NICS(1)_ZZ values of −69.44 and −69.66 ppm, respectively. However, the reversal of aromaticity occurred using NICS(1)_ZZ values of 3.77 and 10.64 ppm in the excited DA1 and PA, respectively, which shows that the S_1 state would return to the ground state by fluorescence emission. For the ground state, the total NICS(1)_ZZ values of *cis*-phenol **HBI-pBr** are similar to DA1 and PA in S_0; thus, the structures experience minimal loss when adding or losing protons. This explains why only small Stokes' shifts are observed for DA1 and PA because no significant change is observed in the equilibrium structure and NICS(1)_ZZ values from the ground to the electronic singlet excited cation and anion, as shown in Fig. 7. Thus, in terms of (*anti*)-aromaticity rationalized, the large Stokes' shifts observed can be attributed to significant changes in the structures and NICS(1)_ZZ values following the ESIPT reaction.[79,80]

Conclusion

In summary, the ground-state and excited-state proton transfer in 2-(2′-hydroxy-5′-bromo)phenylbenzimidazole (**HBI-pBr**) are significantly influenced by solvent and pH conditions. A combination of spectroscopic techniques and a time-dependent density functional theory (TDDFT) approach offers comprehensive mechanistic insights into this intricate process. The mechanism of the ground-state and excited-state proton transfer of **HBI-pBr** was proposed experimentally and theoretically. The maximum absorptions at ~340.0 and 330.0 nm were assigned to the ground *cis*-phenol isomer. The strong FL emission band observed at ~470.0 nm was initiated from the keto of **HBI-pBr**. The monovalent anion and cation were characterized in CH_3OH doped with acid and base, which displayed 416 and 458 nm emission, respectively. *Para*-Bromine substitution localizes the electron distribution in the HBI framework, thereby inhibiting charge transfer.

Finally, both the potential energy surface curves and NICS(1)_ZZ values interpreted the mechanism of ESIPT reaction and formation of cation and anion. This study opens a chapter on the mechanistic understanding of ESIPT through NICS(1)_ZZ values, laying a solid foundation for further designing and developing applications of ESIPT-based fluorescent probes in related fields.

Data availability

The datasets generated and/or analyzed during the current study are available from the corresponding author on reasonable request.

Conflicts of interest

The authors declare that they have no known competing financial interests or personal relationships that could have appeared to influence the work reported in this paper.

Acknowledgements

We gratefully acknowledge the financial support from the National Natural Science Foundation of China (Grant No. 22273086, 21873020 and 21473162). Y. Z. is grateful for support from the Project Grants 521 Talents Cultivation of Zhejiang Sci-Tech University. This work is also supported by the Zhejiang Provincial Top Key Academic Discipline of Chemical Engineering and Technology.

References

1 L. He, B. Dong, Y. Liu and W. Lin, Fluorescent Chemosensors Manipulated by Dual/Triple Interplaying Sensing Mechanisms, *Chem. Soc. Rev.*, 2016, **45**(23), 6449–6461.

2 G.-J. Zhao and K.-L. Han, Hydrogen Bonding in the Electronic Excited State, *Acc. Chem. Res.*, 2012, **45**(3), 404–413.

3 C.-H. Wang, Z.-Y. Liu, C.-H. Huang, C.-T. Chen, F.-Y. Meng, Y.-C. Liao, Y.-H. Liu, C.-C. Chang, E. Y. Li and P.-T. Chou, Chapter Open for the Excited-State Intramolecular Thiol Proton Transfer in the Room-Temperature Solution, *J. Am. Chem. Soc.*, 2021, **143**(32), 12715–12724.

4 D. Schilter, pHotoacids Jump Further, *Nat. Rev. Chem*, 2020, **4**(10), 505.

5 P. Thordarson and J. E. Beves, Confining Photoacidity, *Chem*, 2019, **5**(6), 1366–1368.

6 T. Sun, L. Kang, H. Zhao, Y. Zhao and Y. Gu, Photoacid Generators for Biomedical Applications, *Adv. Sci.*, 2024, **11**(5), e2302875.

7 H. Gu, W. Wang, W. Wu, M. Wang, Y. Liu, Y. Jiao, F. Wang, F. Wang and X. Chen, Excited-State Intramolecular Proton Transfer (ESIPT)-Based Fluorescent Probes for Biomarker Detection: Design, Mechanism, and Application, *Chem. Commun.*, 2023, **59**(15), 2056–2071.

8 C. Bai, J. Zhang, Y. Qin, H. Huang, Z. Xia, Q. Zheng, H. Dai, P. Lu, H. Miao, C. Qu, *et al.*, Precise Probe Design Based ESIPT Coupled AIE Mechanism Toward Endogenous Cyanide in Food Detection and Bioimaging, *Chem. Eng. J.*, 2022, **443**, 136445.

9 X. Wang and C. Ma, A Near-Infrared Fluorescent Chemosensor with a Remarkably Large Stokes Shift for the Ultrasensitive Detection of Tyrosinase Activity and Bioimaging in Living Cells and Mouse Xenograft Model, *Sens. Actuators, B*, 2022, **354**, 131211.

10 C.-C. Yan, X.-D. Wang and L.-S. Liao, Organic Lasers Harnessing Excited State Intramolecular Proton Transfer Process, *ACS Photonics*, 2020, **7**(6), 1355–1366.

11 K. Wu, T. Zhang, Z. Wang, L. Wang, L. Zhan, S. Gong, C. Zhong, Z. Lu, S. Zhang and C. Yang, De Novo Design of Excited-State Intramolecular Proton Transfer Emitters *via* a Thermally Activated Delayed Fluorescence Channel, *J. Am. Chem. Soc.*, 2018, **140**(28), 8877–8886.

12 Y. Wu, R. Wang, R. Lin, X. Xu, X. Zhang, O. Alsalman, Y. Qiu, A. Uddin and X. Ouyang, Excited-State Intramolecular Proton Transfer Emitter for Efficient Violet-Blue Organic Light-Emitting Diodes with Hybridized Local/Charge Transfer Channel, *Chem. Eng. J.*, 2023, **465**, 142929.

13 G. Xiao, Y. J. Ma, X. Fang and D. Yan, Quadruple Anticounterfeiting Encryption: Anion-Modulated Forward and Reverse Excitation-Dependent Multicolor Afterglow in Two-Component Ionic Crystals, *ACS Appl. Mater. Interfaces*, 2022, **14**(26), 30246–30255.

14 Q. Zhang, L. Yang, Y. Han, Z. Wang, H. Li, S. Sun and Y. Xu, A pH-Sensitive ESIPT Molecule with Aggregation-Induced Emission and Tunable Solid-State Fluorescence Multicolor for Anti-Counterfeiting and Food Freshness Detection, *Chem. Eng. J.*, 2022, **428**, 130986.

15 L. Wu, C. Huang, B. P. Emery, A. C. Sedgwick, S. D. Bull, X.-P. He, H. Tian, J. Yoon, J. L. Sessler and T. D. James, Förster Resonance Energy Transfer (Fret)-Based Small-Molecule Sensors and Imaging Agents, *Chem. Soc. Rev.*, 2020, **49**(15), 5110–5139.

16 R. Salaeh and R. Daengngern, Theoretical Insights into Ultrafast Excited State Proton Transfer Coupled with Twisted Intramolecular Charge Transfer Mechanism in 7-(2′-Pyridyl)indole: Effect of Hydrogen Bonding, *J. Mol. Liq.*, 2023, **388**, 122707.

17 S. Ríos Vázquez, J. L. Pérez Lustres, F. Rodríguez-Prieto, M. Mosquera and M. C. Ríos Rodríguez, Excited-State Proton and Charge Transfer in Protonated Amino and

Methylated Derivatives of 2-(2'-Hydroxyphenyl) benzimidazole, *J. Phys. Chem. B*, 2015, **119**(6), 2475–2489.

18 S.-Z. Yi, B.-N. Li, P.-Y. Fu, M. Pan and C.-Y. Su, Interplay of Dual-Proton Transfer Relay to Achieve Full-Color Panel Luminescence in Excited-State Intramolecular Proton Transfer (ESIPT) Fluorophores, *ACS Appl. Mater. Interfaces*, 2023, **15**(2), 3172–3181.

19 Y. Guo, X. Li, J. Ma and D. L. Phillips, Reaction Mechanisms of Photoinduced Quinone Methide Intermediates Formed *via* Excited-State Intramolecular Proton Transfer or Water-Assisted Excited-State Proton Transfer of 4-(2-Hydroxyphenyl)pyridine, *J. Phys. Chem. Lett.*, 2021, **12**(48), 11666–11672.

20 Z. Li, Z. Tang, W. Li, H. Zhan, X. Liu, Y. Wang, J. Tian and X. Fei, Substituents Effect on the Methanol-Assisted Excited-State Intermolecular Proton Transfer of 7-Aminoquinoline: A theoretical study, *J. Mol. Liq.*, 2021, **341**, 116920.

21 Y. Chen, Y. Fang, H. Gu, J. Qiang, H. Li, J. Fan, J. Cao, F. Wang, S. Lu and X. Chen, Color-Tunable and ESIPT-Inspired Solid Fluorophores Based on Benzothiazole Derivatives: Aggregation-Induced Emission, Strong Solvatochromic Effect, and White Light Emission, *ACS Appl. Mater. Interfaces*, 2020, **12**(49), 55094–55106.

22 G. K. Weragoda, N. M. Abdelaziz, D. Govorov, R. Merugu, L. J. Patton, J. E. Grabo, R. A. A. U. Ranaweera, A. C. Ratliff, W. D. Mendis, N. Ahmed, *et al.*, Excited-State Intramolecular Proton Transfer in Salicylidene-α-Hydroxy Carboxylate Derivatives: Direct Detection of the Triplet Excited State of the *cis*-Keto Tautomer, *J. Phys. Chem. A*, 2023, **127**(12), 2765–2778.

23 B. C. Dickinson and C. J. Chang, A Targetable Fluorescent Probe for Imaging Hydrogen Peroxide in the Mitochondria of Living Cells, *J. Am. Chem. Soc.*, 2008, **130**(30), 9638–9639.

24 S. Zhong, S. Huang, B. Feng, T. Luo, F. Chu, F. Zheng, Y. Zhu, F. Chen and W. Zeng, An ESIPT-Based AIE Fluorescent Probe to Visualize Mitochondrial Hydrogen Peroxide and Its Application in Living Cells and Rheumatoid Arthritis, *Org. Biomol. Chem.*, 2023, **21**(24), 5063–5071.

25 Z. Li, Y. Wu, Y. Shen and B. Gu, Simple NIR-Emitting ESIPT Fluorescent Probe for Thiophenol with a Remarkable Stokes Shift and Its Application, *ACS Omega*, 2020, **5**(19), 10808–10814.

26 G. Zeng, Z. Liang, X. Jiang, T. Quan and T. Chen, An ESIPT-Dependent AIE Fluorophore Based on HBT Derivative: Substituent Positional Impact on Aggregated Luminescence and Its Application for Hydrogen Peroxide Detection, *Chem.–Eur. J.*, 2022, **28**(5), e202103241.

27 G. Mazzeo, M. Fusè, A. Evidente, S. Abbate and G. Longhi, Circularly Polarized Luminescence of Natural Products Lycorine and Narciclasine: Role of Excited-State Intramolecular Proton-Transfer and Test of pH Sensitivity, *Phys. Chem. Chem. Phys.*, 2023, **25**(34), 22700–22710.

28 T. Kumpulainen, B. Lang, A. Rosspeintner and E. Vauthey, Ultrafast Elementary Photochemical Processes of Organic Molecules in Liquid Solution, *Chem. Rev.*, 2017, **117**(16), 10826–10939.

29 V. Khorwal and R. J. S. C. Kathuria, Protonation–Deprotonation Dynamics of 2-(4′-Pyridyl)benzimidazole Derivative with Cucurbit[6]uril at Two Different pH, *Supramol. Chem.*, 2021, **33**, 452–459.

30 M. Das, M. Brahma and G. Krishnamoorthy, Controlling the Photoswitching of 2-(4′-Diethylamino-2′-hydroxyphenyl)-1H-imidazo-[4,5-*b*]pyridine by pH, *J. Photochem. Photobiol., A*, 2021, **421**, 113504.

31 S. K. Dogra, Spectral Characteristics of 2-(2′-Hydroxy-3′-pyridyl)benzimidazole: Effects of Solvents and Acid or Base Concentrations, *J. Mol. Struct.*, 2005, **734**(1), 51–60.

32 C. Prommin, N. Kanlayakan, W. Chansen, R. Salaeh, K. Kerdpol, R. Daengngern and N. Kungwan, Theoretical Insights on Solvent Control of Intramolecular and Intermolecular Proton Transfer of 2-(2′-Hydroxyphenyl) benzimidazole, *J. Phys. Chem. A*, 2017, **121**(31), 5773–5784.

33 X. Liu, M. Cheng, L. Yang, M. Wang, Y. Yang and J. Han, Theoretical Study on the Effect of Naphthalene Modifications on the ESIPT Mechanism and Photophysical Properties of Benzimidazoles, *J. Lumin.*, 2024, **269**, 120495.

34 A. Malakar, F. A. S. Chipem and G. Krishnamoorthy, Perturbation of Proton Transfer of 2-(2′-Hydroxyphenyl) benzimidazole and Its Nitrogenous Analogues by Nanoparticles, *J. Mol. Struct.*, 2020, **1217**, 128352.

35 W.-Z. Bi, Y. Geng, W.-J. Zhang, C.-Y. Li, C.-S. Ni, Q.-J. Ma, S.-X. Feng, X.-L. Chen and L.-B. Qu, Highly Sensitive and Selective Detection of Triphosgene with a 2-(2′-Hydroxyphenyl)benzimidazole Derived Fluorescent Probe, *RSC Adv.*, 2023, **13**(44), 30771–30776.

36 Z.-J. Li, W.-J. Zhang, W.-Z. Bi, Q.-J. Ma, S.-X. Feng, X.-L. Chen and L.-B. Qu, An Amino-Substituted 2-(2′-Hydroxyphenyl) benzimidazole for the Fluorescent Detection of Phosgene Based on an ESIPT Mechanism, *RSC Adv.*, 2021, **11**(18), 10836–10841.

37 J. Wang, Y. Li and Y. Pang, A Step Toward an NIR-Emitting ESIPT Probe for Smart Zn^{2+} Sensing in Different Environments, *Chem. Biomed. Imaging*, 2023, **1**(6), 537–540.

38 G. Sun and H. Fang, Computational Insights into Sensing Mechanism for Al^{3+} in a New Acylhydrazone Fluorescent Probe Based on Excited-State Intramolecular Proton Transfer (ESIPT) and Twisted Intramolecular Charge Transfer (TICT), *J. Phys. Chem. A*, 2023, **127**(8), 1857–1865.

39 N. Nehra and R. Kaushik, ESIPT-Based Probes for Cations, Anions and Neutral Species: Recent Progress, Multidisciplinary Applications and Future Perspectives, *Anal. Methods*, 2023, **15**(40), 5268–5285.

40 M. Coehlo, G. Clavier and G. Pieters, Excited State Intramolecular Proton Transfer Based Fluorophores with Circularly Polarized Luminescence Emission, *Adv. Opt. Mater.*, 2022, **10**(4), 2101774.

41 X. Lv, J. Song, S. Guo, J. Gu, L. Meng and C.-Z. Lu, Enhancing Reverse Intersystem Crossing in Triptycene-TADF Emitters: Theoretical Insights into Reorganization Energy and Heavy Atom Effects, *J. Phys. Chem. A*, 2024, **128**(9), 1611–1619.

42 R. Okumura, H. Tanaka, K. Shizu, S. Fukushima, Y. Yasuda and H. Kaji, Development of an Organic Emitter Exhibiting

Reverse Intersystem Crossing Faster than Intersystem Crossing, *Angew. Chem., Int. Ed.*, 2024, e202409670.

43 M. G. Holler, L. F. Campo, A. Brandelli and V. Stefani, *J. Photochem. Photobiol., A*, 2002, **149**, 217–225.

44 A. D. Becke, Density-Functional Thermochemistry. III. The Role of Exact Exchange, *J. Phys. Chem.*, 1993, **98**(7), 5648–5652.

45 P. J. Stephens, F. J. Devlin, C. F. Chabalowski and M. J. Frisch, *Ab Initio* Calculation of Vibrational Absorption and Circular Dichroism Spectra Using Density Functional Force Fields, *J. Phys. Chem.*, 1994, **98**(45), 11623–11627.

46 A. D. Becke, Density-Functional Thermochemistry. IV. A New Dynamical Correlation Functional and Implications for Exact-Exchange Mixing, *J. Phys. Chem.*, 1996, **104**(3), 1040–1046.

47 E. Runge and E. K. U. Gross, Density-Functional Theory for Time-Dependent Systems, *Phys. Rev. Lett.*, 1984, **52**(12), 997–1000.

48 R. Bauernschmitt and R. Ahlrichs, Treatment of Electronic Excitations Within the Adiabatic Approximation of Time Dependent Density Functional Theory, *Chem. Phys. Lett.*, 1996, **256**, 454–464.

49 M. E. Casida, C. Jamorski, K. C. Casida and D. R. Salahub, Molecular Excitation Energies to High-Lying Bound States from Time-Dependent Density-Functional Response Theory: Characterization and Correction of the Time-Dependent Local Density Approximation Ionization Threshold, *J. Chem. Phys.*, 1998, **108**, 4439–4449.

50 R. E. Stratmann, G. E. Scuseria and M. J. Frisch, An Efficient Implementation of Time-Dependent Density-Functional Theory for the Calculation of Excitation Energies of Large Molecules, *J. Chem. Phys.*, 1998, **109**, 8218–8224.

51 F. Furche and R. Ahlrichs, Adiabatic Time-Dependent Density Functional Methods for Excited State Properties, *J. Chem. Phys.*, 2002, **117**, 7433–7447.

52 M. A. L. Marques and E. K. U. Gross, Time-Dependent Density Functional Theory, *Annu. Rev. Phys. Chem.*, 2004, **55**, 427–455.

53 M. Chiba, T. Tsuneda and K. Hirao, Excited State Geometry Optimizations by Analytical Energy Gradient of Long-Range Corrected Time-Dependent Density Functional Theory, *J. Chem. Phys.*, 2006, **124**, 144106.

54 M. E. Casida, Time-Dependent Density-Functional Theory for Molecules and Molecular Solids, *J. Mol. Struct.:THEOCHEM*, 2009, **914**, 3–18.

55 M. A. Marques and E. K. Gross, Time-Dependent Density Functional Theory, *Annu. Rev. Phys. Chem.*, 2004, **55**, 427–455.

56 M. J. Frisch, J. A. Pople and J. S. Binkley, Self-Consistent Molecular Orbital Methods 25. Supplementary Functions for Gaussian Basis Sets, *J. Chem. Phys.*, 1984, **80**(7), 3265–3269.

57 C. Amovilli, V. Barone, R. Cammi, E. Cancès, M. Cossi, B. Mennucci, C. S. Pomelli and J. Tomasi, Recent Advances in the Description of Solvent Effects with the Polarizable Continuum Model, *Adv. Quantum Chem.*, 1998, **32**, 227–261.

58 (*a*) K. Fukui, Formulation of the Reaction Coordinate, *J. Phys. Chem.*, 1970, **74**(23), 4161–4163; (*b*) K. Fukui, The Path of Chemical Reactions-the IRC Approach, *Acc. Chem. Res.*, 1981, **14**(12), 363–368.

59 R. West, J. J. Buffy and M. Haaf, Chemical Shift Tensors and NICS Calculations for Stable Silylenes, *J. Am. Chem. Soc.*, 1998, **120**(7), 1639–1640.

60 J. Polkaehn, R. Molenda and M. A. Cordero, Synthesis and Properties of 5,7-Diazaullazines, *J. Org. Chem.*, 2024, **89**(4), 2169–2181.

61 N. C. Baird, Quantum Organic Photochemistry. II. Resonance and Aromaticity in the Lowest $^3\pi\pi^*$ State of Cyclic Hydrocarbons, *J. Am. Chem. Soc.*, 1972, **94**(14), 4941–4948.

62 P. V. R. Schleyer, C. Maerker, A. Dransfeld, H. Jiao and N. J. R. van Eikema Hommes, Nucleus-Independent Chemical Shifts: A Simple and Efficient Aromaticity Probe, *J. Am. Chem. Soc.*, 1996, **118**(26), 6317–6318.

63 D. Dunlop, L. Ludvíková, A. Banerjee, H. Ottosson and T. Slanina, Excited-State (Anti)Aromaticity Explains Why Azulene Disobeys Kasha's Rule, *J. Am. Chem. Soc.*, 2023, **145**(39), 21569–21575.

64 J. J. Blackner, O. M. Schneider and W. O. Wong, Removing Neighboring Ring Influence in Monocyclic B–OH Diazaborines: Properties and Reactivity as Phenolic Bioisosteres with Dynamic Hydroxy Exchange, *J. Am. Chem. Soc.*, 2024, **146**(28), 19499–19508.

65 M. J. Frisch; G. W. Trucks; H. B. Schlegel; G. E. Scuseria; M. A. Robb; J. R. Cheeseman; G. Scalmani; V. Barone; B. Mennucci; G. A. Petersson; H. Nakatsuji; M. Caricato; X. Li; H. P. Hratchian; A. F. Izmaylov; J. Bloino; G. Zheng; J. L. Sonnenberg; M. Hada; M. Ehara; K. Toyota; R. Fukuda; J. Hasegawa; M. Ishida; T. Nakajima; Y. Honda; O. Kitao; H. Nakai; T. Vreven; J. A. Jr. Montgomery; J. E. Peralta; F. Ogliaro; M. Bearpark; J. J. Heyd; E. Brothers; K. N. Kudin; V. N. Staroverov; R. Kobayashi; J. Normand; K. Raghavachari; A. Rendell; J. C. Burant; S. S. Iyengar; J. Tomasi; M. Cossi; N. Rega; J. M. Millam; M. Klene; J. E. Knox; J. B. Cross; V. Bakken; C. Adamo; J. Jaramillo; R. Gomperts; R. E. Stratmann; O. Yazyev; A. J. Austin; R. Cammi; C. Pomelli; J. W. Ochterski; R. L. Martin; K. Morokuma; V. G. Zakrzewski; G. A. Voth; P. Salvador; J. J. Dannenberg; S. Dapprich; A. D. Daniels; Ö. Farkas; J. B. Foresman; J. V. Ortiz; J. Cioslowski; D. J. Fox *Gaussian 09, Revision D.01*; Gaussian, Inc., Wallingford CT, 2009.

66 Y. Guo, Z. Cai, F. Yan, D. Lei, Y. Guo, S. Zhang and X. Dou, Precise Electron-Withdrawing Strength Modulation of ESIPT Probes for Ultrasensitive and Specific Fluorescence Sensing, *Anal. Chem.*, 2023, **95**(23), 9014–9024.

67 H. Ren, F. Huo, X. Wu, X. Liu and C. Yin, An ESIPT-Induced NIR Fluorescent Probe to Visualize Mitochondrial Sulfur Dioxide During Oxidative Stress in Vivo, *Chem. Commun.*, 2021, **57**(5), 655–658.

68 R. Omidyan and M. Iravani, Excited State Proton Transfer and Deactivation Mechanism of 2-(4′-Amino-2′-hydroxyphenyl)-1H-imidazo-[4,5-c]pyridine and Its

Analogues: A Theoretical Study, *J. Phys. Chem. A*, 2016, **120**(7), 1012–1019.

69 M. Das, M. Brahma and G. Krishnamoorthy, Light-Driven Switching between Intramolecular Proton-Transfer and Charge-Transfer States, *J. Phys. Chem. B*, 2021, **125**(9), 2339–2350.

70 M. Vidal, M. C. Rezende, C. Pastene, C. Aliaga and M. Domínguez, Solvatochromism of Conjugated 4-N,N-Dimethylaminophenyl-pyridinium Donor-Acceptor Pairs, *New J. Chem.*, 2018, **42**(6), 4223–4231.

71 Y. Yang, Y. Ding and W. Shi, The effects of amino group *meta*-and *para*-substitution on ESIPT mechanisms of amino 2-(2′-hydroxyphenyl)benzazole derivatives, *J. Lumin.*, 2020, **218**, 116836–116846.

72 C. Li, Y. Yang and C. Ma, Effect of amino group on the excited-state intramolecular proton transfer (ESIPT) mechanisms of 2-(2′-hydroxyphenyl)benzoxazole and its amino derivatives, *RSC Adv.*, 2016, **6**, 5134–5140.

73 Y. Li, Y. Wang, X. Feng and Y. Zhao, Spectroscopic and Mechanistic Insights into Solvent Mediated Excited-State Proton Transfer and Aggregation-Induced Emission: Introduction of Methyl Group onto 2-(*o*-Hydroxyphenyl) benzoxazole, *Phys. Chem. Chem. Phys.*, 2022, **24**(42), 26297–26306.

74 P.-Y. Fu, B.-N. Li, Q.-S. Zhang, J.-T. Mo, S.-C. Wang, M. Pan and C.-Y. Su, Thermally Activated Fluorescence *vs* Long Persistent Luminescence in ESIPT-Attributed Coordination Polymer, *J. Am. Chem. Soc.*, 2022, **144**(6), 2726–2734.

75 J. Hao and Y. Yang, Theoretical Investigation of the Excited-State Dynamics Mechanism of the Asymmetric Two-Way Proton Transfer Molecule BTHMB, *J. Phys. Chem. A*, 2021, **125**(48), 10280–10290.

76 N. A. Shekhovtsov and M. B. Bushuev, Enol or keto? Interplay Between Solvents and Substituents as a Factor Controlling ESIPT, *J. Mol. Liq.*, 2022, **361**, 119611.

77 M.-A. Codescu, M. Weiß, M. Brehm, O. Kornilov, D. Sebastiani and E. T. J. Nibbering, Switching Between Proton Vacancy and Excess Proton Transfer Pathways in the Reaction between 7-Hydroxyquinoline and Formate, *J. Phys. Chem. A*, 2021, **125**(9), 1845–1859.

78 M. K. Saroj, R. Payal, S. K. Jain and R. C. Rastogi, Study of Prototropic Reactions of Indole Chalcone Derivatives in Ground and Excited States Using Absorption and Fluorescence Spectroscopy, *J. Mol. Liq.*, 2020, **302**, 112164.

79 C.-H. Wu, L. J. Karas, H. Ottosson and J. I. C. Wu, Excited-State Proton Transfer Relieves Antiaromaticity in Molecules, *Proc. Natl. Acad. Sci. U. S. A.*, 2019, **116**(41), 20303–20308.

80 B. Oruganti, J. Wang and B. Durbeej, Modulating the Photocyclization Reactivity of Diarylethenes through Changes in the Excited-State Aromaticity of the π-Linker, *J. Org. Chem.*, 2022, **87**(17), 11565–11571.